

# Role of Matrix Microstructure on Room-Temperature Tensile Properties and Fiber-Strength Utilization of an Orthorhombic Ti-Alloy-Based Composite

C.J. BOEHLERT, B.S. MAJUMDAR, S. KRISHNAMURTHY, and D.B. MIRACLE

Microstructure-property understanding obtained for a nominally Ti-25Al-17Nb (at. pct) monolithic sheet alloy was used to heat treat a unidirectional four-ply SCS-6/Ti-25Al-17Nb metal-matrix composite (MMC) and a fiberless “neat” material of the same alloy for enhancing mechanical properties. The unreinforced alloy and  $[0]_4$  composite recorded significant improvements in ductility and strength, which were related to the microstructural condition. Modeling of the tensile strength based on fiber fracture statistics helped in understanding how improved matrix microstructure provided more efficient utilization of fiber strength. In comparison to the  $[0]_4$  MMC, improvement of the  $[90]_4$  response was negligible, which was related to an  $\alpha_2$  stabilized zone around the fiber. A Nb coating on the fiber was used to modify the local microstructure, and it produced a modest improvement in strength and ductility in the transverse direction. Structure-property relations of the matrix under different heat-treatment conditions are described in terms of deformation and failure mechanisms of the constituent phases;  $\alpha_2$  (ordered hexagonal close-packed), B2 (ordered body-centered cubic), and O (ordered orthorhombic based on  $\text{Ti}_2\text{AlNb}$ ).

## I. INTRODUCTION

Recently, there has been considerable interest in Nb-rich  $\text{Ti}_3\text{Al}$  alloys due to the discovery of an orthorhombic (O) phase based on the compound  $\text{Ti}_2\text{AlNb}$ .<sup>[1]</sup> This O phase, first found in a Ti-25Al-12.5Nb (at. pct)\* alloy, is similar

Alloy compositions are given in atomic percent unless otherwise stated.

in nature to  $\alpha_2$  ( $\text{Ti}_3\text{Al}$ ,  $\text{DO}_{19}$  structure), yet differs by the lattice arrangement of Nb with respect to Ti.<sup>[1,2]</sup> The atomic positions on the basal planes of the  $\alpha_2$  and O lattices, based on findings in Reference 2, are sketched to scale in Figure 1, which shows how the ordered arrangement of the different-sized Nb and Ti atoms have destroyed the hexagonal symmetry of the  $\alpha_2$  phase. The O phase has been identified in Ti-alloy compositions ranging from 20 to 30 Al and 11 to 30 Nb,<sup>[3,4]</sup> and such alloys are often referred to as O alloys. The O alloys, such as Ti-22Al-23Nb, have outperformed  $\alpha_2$  alloys in terms of creep, tensile strength, ductility, and thermomechanical fatigue (TMF).<sup>[5,6,7]</sup> Enhanced tensile strength, TMF, and toughness have also been shown for a lighter alloy, nominally Ti-25Al-17Nb.<sup>[8-11]</sup>

Because of their attractive combination of room-temperature (RT) ductility and elevated temperature strength, O alloys are being considered as matrix alloys for continuously reinforced metal-matrix composites (MMCs). Additional advantages of O-based systems have included less environmental sensitivity of the alloys to interstitial content (primarily oxygen) and reduced reactivity with SiC fibers.<sup>[9]</sup> The longitudinal and transverse strengths and creep resistance are important properties for MMCs and, unlike poly-

meric composites, the matrix plays a key role in these properties.<sup>[12]</sup> In an earlier work on a  $[0]_4$  SCS-6/Ti-25Al-17Nb MMC, the as-processed  $[0]_4$  MMC barely met the rule-of-mixtures strength, and the  $[90]_4$  MMC had poor strength and strain-to-failure.<sup>[9]</sup> The matrix microstructure of the MMC was suspected to be largely responsible for the poor tensile properties, and this prompted the need to modify the matrix microstructure of the composite to improve mechanical properties. It is demonstrated in this article that matrix ductility, which is dependent on the heat treatment and its associated matrix microstructure, significantly influences efficient utilization of fiber strength during longitudinal loading of MMCs. To our knowledge, such a direct influence of matrix ductility on fiber strength utilization has not been established before.

The objectives of this work were twofold: (1) to understand microstructure-property relationships of the O alloy in fiberless form, and (2) to use this understanding to implement a beneficial matrix microstructure in MMCs for better fiber-strength utilization. The approach was to initially probe the microstructure-property relationships of a nominally Ti-25Al-17Nb monolithic alloy by performing heat treatments and mechanical testing of the precursor sheet material. This was followed by evaluation of a fiberless “neat” material obtained by consolidation of thin foils. Based on results from the sheet and neat materials, a heat treatment was selected for the consolidated SCS-6/Ti-25Al-17Nb MMC for property improvements. Modeling of longitudinal strength of the composite was conducted to help understand the effect of matrix ductility on longitudinal strength of the MMC. In addition, because heat treatments were unable to provide required improvements in the transverse (90 deg) properties, a Nb coating was applied to the fibers prior to composite fabrication in order to evaluate the effect of a modified matrix microstructure in the near-fiber region on transverse behavior.

C.J. BOEHLERT, Materials Scientist, and B.S. MAJUMDAR and S. KRISHNAMURTHY, Senior Scientists, are with UES, Inc. Dayton, OH 45432-1894. D.B. MIRACLE, Research Group Leader, is with the Wright Laboratory Materials Directorate, Wright-Patterson AFB, OH 45433-7817.

Manuscript submitted March 11, 1996.

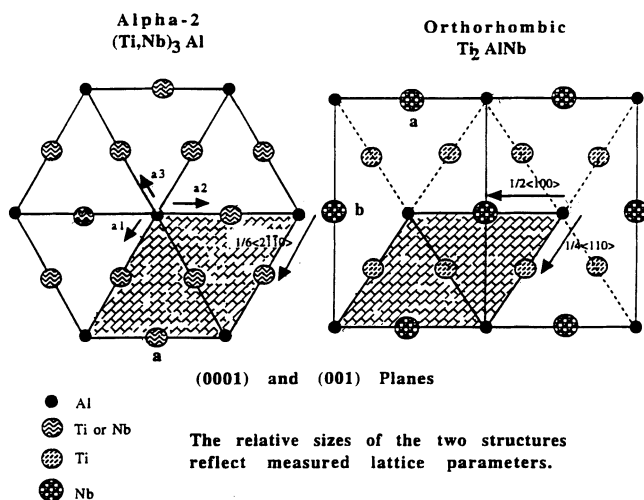


Fig. 1—Atomic positions on the basal planes of the  $\alpha_2$  and O lattices.

## II. EXPERIMENTAL PROCEDURES

The monolithic materials used in this study were obtained from sheets produced by Timet, Inc. (Henderson, Nev.) Ingots were forged in the  $\beta$ -phase region, followed by cross-rolling in the  $\alpha_2$  + B2-phase region at 1010 °C to a nominal thickness of 2 mm. This constituted the “sheet” material in this study. Other sheets were ground and unidirectional cold-rolled to a final foil thickness of 125  $\mu$ m by Texas Instruments (Attleboro, MA). Foils were then consolidated into a four-ply neat format by Textron Specialty Materials Division (Lowell, MA) using a hot isostatic pressing (HIP) cycle consisting of a pressure of 103 MPa at 940 °C for 6 hours. The composite panels were fabricated using a four-ply foil-fiber-foil layup with Textron’s SCS-6 fibers and an identical HIP cycle.

Sheet specimens were heat treated in better than  $10^{-6}$  torr vacuum. Typical heat treatments, diagramed in Figure 2, consisted of two stages: a higher-temperature solution treatment either above the  $\beta/\text{B2}$  transus or in the  $\alpha_2$  + B2 phase field, followed by a lower-temperature aging treatment to nucleate and grow the O phase. It should be noted that no attempt was made to distinguish between the  $\beta$  and B2 phases. To guide selection of suitable solutionizing temperatures for appropriately changing  $\alpha_2$  volume fractions, an estimate of the two-phase  $\alpha_2$  and B2 phase boundaries was obtained initially by solutionizing sheet specimens at temperatures ranging between 1000 °C and 1150 °C for 200 hours and then water quenching. The compositions of the constituent phases were then used to approximately determine the two-phase field boundaries. Figure 2(a) represents a super  $\beta/\text{B2}$  transus solution treatment followed by air quenching and aging, while Figure 2(b) illustrates a subtransus solution treatment followed by a controlled cool (CC) at 28 °C per minute to the aging temperature. In addition, a few specimens were rapidly quenched in order to prevent formation of O phase. Because the solutionizing temperature appeared to have the more dominant effect on properties over any subsequent treatment, the three-step heat treatment involving solutionizing, cooling, and aging will be specified only by the solution treatment temperature.

Neat and composite specimens were subjected to a 1050 °C solutionizing heat treatment, diagramed in Figure 2(b)

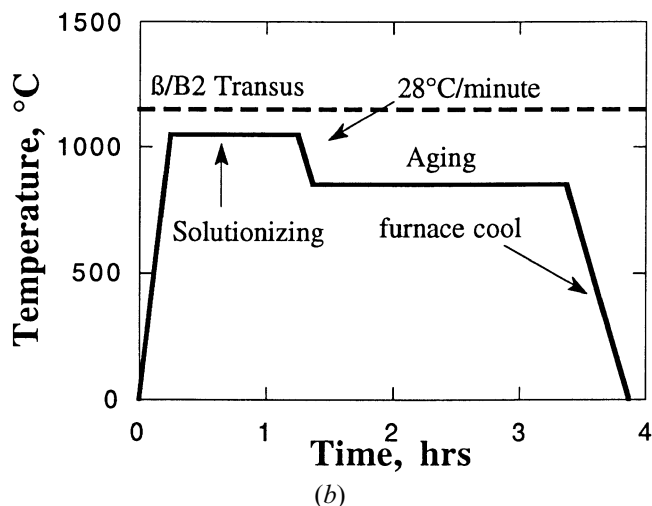
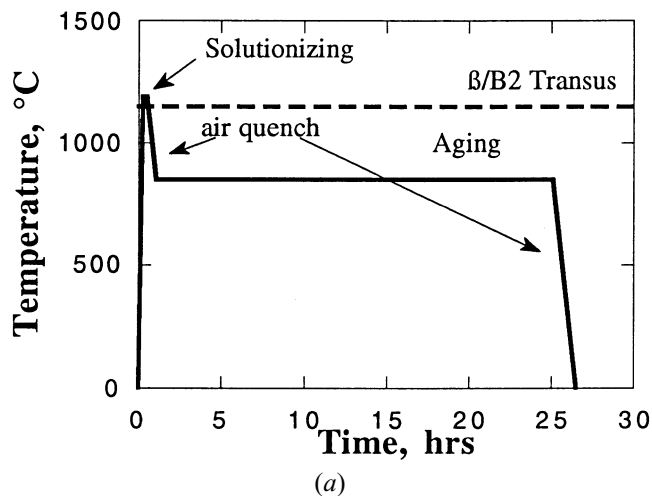


Fig. 2—Sketches illustrating the (a) supertransus and (b) subtransus heat treatments.

because it provided significant improvements in the tensile and creep performance of the sheet material.<sup>[13,14,15]</sup> Prior to mechanical testing, the sheets and panels were either electrodischarge machined (EDM) or diamond wheel cut to “dog-bone” or rectangular specimen geometries and ground through sequentially finer grids of SiC paper to remove surface contaminants and EDM-affected layers. Some sheet specimens were mechanically polished to a better than 1- $\mu$ m finish to reveal surface slip traces. Testing was performed at RT on an Instron 8500 servohydraulic mechanical testing machine at a strain rate of  $10^{-4}$ /s. The microstructures, slip behavior, and fracture morphology were evaluated using optical microscopy, a Leica 360 FE scanning electron microscope (SEM), a JEOL\* 733 electron

\*JEOL is a trademark of Japan Electron Optics Ltd., Tokyo.

microprobe, and a Hitachi 100 kV transmission electron microscope (TEM). In addition, selected X-ray diffraction studies were performed to confirm the microstructural observations. Volume fraction analysis of the constituent phases was performed using NIH image analysis software on high-contrast, digitized backscattered SEM images.

In order to determine the fiber-strength characteristics in the composite and help clarify the events leading to final

fracture of the MMC, fibers were extracted from the heat-treated composite by chemically dissolving the matrix in a Kroll's reagent. Mechanical tests were performed on the extracted fibers over a gage length of 25.4 mm at a strain rate of 0.0133/s. A total of 50 fibers that failed within the gage length were used to determine the Weibull modulus ( $m$ ) and the reference strength ( $\sigma_0$ ) according to Weibull statistics.

In addition, a single-ply composite was fabricated that contained SCS-6 fibers that were coated with approximately 4  $\mu$ -thick Nb. The reason for the coating was to modify the matrix microstructure in the near-fiber region in a further attempt to improve the transverse (90 deg) strength and strain-to-failure of the composite. The coating was deposited using the plasma vapor deposition (PVD) process. The fabrication procedure included a 1-hour hold at 1050 °C followed by a controlled cool of 10 °C per minute to 850 °C and a subsequent hold for 2-hours. A constant pressure of 103 MPa was maintained during the entire processing cycle, and it should be noted that the HIP cycle resembled the heat treatment used on the fiberless alloys and [0]<sub>4</sub> composites (Figure 2(b)).

### III. MODELING THE STRENGTH OF 0-DEG MMCS

This section is devoted to modeling of the 0 deg MMC strength based on constitutive properties of the fiber, matrix, and interface. Such modeling is important because comparisons of predicted and measured strengths of the MMC provide clearer understanding of the influence of matrix ductility on utilization of fiber strength. Additionally, such comparisons help to illuminate the likely sequence of events leading to final failure of the MMC.

At failure, the stress in the composite is

$$\sigma_{MMC} = v_f \cdot \sigma_{uf} + (1 - v_f) \cdot \sigma_{um} \quad [1]$$

where  $v_f$  is the volume fraction of the fiber and  $\sigma_{uf}$  and  $\sigma_{um}$  are the stresses carried by the fiber and matrix, respectively, at failure.

The strength contribution of the matrix is straightforward, because it is almost always yielded. The more critical problem is to estimate the fiber strength based on statistical considerations. The fiber-strength estimate is dependent on the assumed scenario of failure. Pertinent equations are provided below for four models of fiber failure:

- (a) dry bundle strength,
- (b) strength based on Curtin's [16] global load-sharing model,
- (c) strength based on occurrence of the first fiber failure, and
- (d) strength based on two breaks and accompanied stress concentration (Zweben's and Rosen's<sup>[17]</sup> model).

One of the lowest fiber-strength estimates is the dry bundle strength, wherein the failure of a fiber at any one location is tantamount to loss of use of that entire fiber. This is also equivalent to assuming zero friction stress at the interface. The dry bundle fiber strength,  $\sigma_{dbf}$ , is given by<sup>[18]</sup>

$$\sigma_{dbf} = \sigma_0 / (m e L / L_0)^{1/m} \quad [2]$$

where  $\sigma_0$  and  $m$  are the Weibull strength and shape factor (Weibull modulus) for the fibers, respectively,  $e$  is the ex-

ponential term ( $=2.7183$ ),  $L$  is the length of the bundle (equal to the gage length of the MMC sample), and  $L_0$  is the gage length of fibers over which the Weibull parameters are based. The probability of failure ( $P_f$ ) of a fiber of length  $L$  is given by

$$P_f = 1 - \exp \{ -(L/L_0) \cdot (\sigma/\sigma_0)^m \} \quad [3]$$

At RT with reasonably high friction stresses, a dry bundle strength does not appear to be appropriate, because the fiber regains its load carrying capability at a fairly short distance ( $\approx 1$  mm) from the fiber break. At high temperatures, however, where clamping stresses are small, the dry bundle strength may become appropriate.

A more realistic situation at RT is the ability of a broken fiber to recarry the load after a sliding distance  $\delta$  from the fiber crack. In this case, the friction stress plays a role, and an upper bound strength of fibers is obtained by assuming global load sharing (no stress concentrations). Using Curtin's model,<sup>[16]</sup> the fiber strength under global load sharing  $\sigma_{glf}$  is given by

$$\sigma_{glf} = \sigma_c \cdot [ \{ 2/(m+2) \}^{1/(m+1)} ] \cdot [(m+1)/(m+2)] \quad [4]$$

where the characteristic strength  $\sigma_c$  is given by

$$\sigma_c = \{ \sigma_0^m \cdot \tau \cdot L_0 / r \}^{1/(m+1)} \quad [5]$$

Here,  $\tau$  is shear stress (friction stress) at the interface required for fiber/matrix sliding. The term  $\sigma_{glf}$  represents an upper bound strength for fibers, because it neglects stress concentrations associated with broken fibers. The model also provides estimates of the expected number of random fiber breaks. Thus, 10 to 20 pct of fibers are typically estimated to be broken randomly over each characteristic shear lag distance (1.5 to 3 mm) for the SCS-6/Ti-alloy system considered. These values represent a fairly large number of random breaks over the entire gage length of the MMC sample.

A third possibility is to assume that in a low-ductility matrix, failure would ensue on the formation of the first fiber break. The mechanism is explained as follows. Even with a weak interface strength, a high strain concentration occurs in the matrix immediately adjacent to a fiber break.<sup>[19]</sup> For a matrix of low ductility, this can nucleate a matrix crack at that location and propagate rapidly to the next fiber. That fiber now has to support the load originally carried by the broken fiber and the adjacent matrix, and there is also the stress concentration associated with the matrix crack. If the far-field stress in the adjacent fiber is already high, then the additional stress concentration can potentially lead to its failure. The chain of events would continue until complete failure of the composite. Even if the fiber adjacent to the original fiber break were to bridge, continued propagation of the matrix crack at high applied loads can quickly overstress the fiber in its wake and lead to its failure. This is similar to the progression from a bridged crack to an unbridged crack in a fatigue crack growth situation.

An estimate of the stress required for the first fiber crack follows directly from Eq. [3], where the expected number of breaks  $N_b$  in a fiber of total length  $L_i$  is simply

$$N_b = (L_i/L_0) \cdot (\sigma/\sigma_0)^m \quad [6]$$

Equating  $N_b$  to unity, we obtain the fiber stress for the first

fiber break  $\sigma_{\text{fbr}}$  as

$$\sigma_{\text{fbr}} = \sigma_0 \cdot \{L_0/(L \cdot N_f)\}^{1/m} \quad [7]$$

where  $N_f$  is the total number of fibers in the gage length  $L$  of the MMC test specimen. Note that, similar to the dry bundle model, the fiber stress is inversely related to the gage length of the sample. Actually, there is an inverse dependency on the total fiber volume fraction involved.

The fourth failure criteria is based on occurrence of two fiber breaks.<sup>[17]</sup> In this scenario, a stress concentration is generated in a fiber adjacent to the first fiber break without cracking of the intervening matrix. If the adjacent fiber fails based on probability considerations, then it is assumed that the composite would also fail. The concept was put forth by Zweben and Rosen,<sup>[17]</sup> where it was shown that it did provide good agreement with the strength measured for boron-fiber-reinforced aluminum composites. The model emphasizes the issue of stress concentration associated with a fiber break, and it predicts much fewer fiber breaks in a sample, as compared with the Curtin model.<sup>[16]</sup> It was shown in Reference 17 that the difference in the applied stress for three or more breaks compared with the two-break situation was rather small for the boron fibers; *i.e.*, after two adjacent fractures, the stress is sufficient, through stress concentration, to sustain a succession of breaks with only a small increase required for the applied stress.

The last model is attractive for matrix materials of limited ductility, in the 3 to 5 pct elongation-to-failure level, or those that plastically deform with sharp shear bands, such as when stress concentrations dominate and fiber fractures become localized.<sup>[20,21]</sup> Using the results in Reference 17, the pertinent equation for the fiber stress corresponding to the second fiber fracture  $\sigma_{\text{sfrr}}$  is

$$\{\delta \cdot L/L_0^2\} \cdot N_f \cdot C \cdot (\sigma_{\text{sfrr}}/\sigma_0)^{2m} = 1 \quad [8]$$

where  $\delta$  is the shear lag distance and  $C$  is a constant. The value  $\delta$  is dependent upon the fiber diameter  $d$ , the friction stress of the fiber-matrix interface  $\tau$ , and the fiber stress  $\sigma_f$ , according to

$$\delta = \sigma_f \cdot d/4\tau \quad [9]$$

and  $C$  is given by

$$C = 4 \cdot \{k^m - 1\} \quad [10]$$

where  $k$  is the stress concentration factor for one fiber break and is equal to 1.146.<sup>[22]</sup> In this model, a larger friction stress produces a smaller shear lag distance requiring a larger fiber stress at MMC fracture. Although the fiber stress depends on the fiber volume fraction, the dependence is moderated by a power of  $(-1/(2m))$ , which is quite small for the SiC fibers considered for MMC applications. In any case, the dependence of MMC strength on length and the number of fibers provides added means of establishing which of the mechanisms is actually operative.

It also is notable, with respect to the last model, that, when the stress concentration factor is high (such as when a matrix crack is propagating from the first fiber break), the stress calculated from Eq. [9] can fall below that for the first fiber break. Thus, the maximum failure stress is then governed by the first fiber break. For fiber-strength parameters, which will be discussed later in Section V, the tran-

sition from a second-break to a first-break dominated failure can occur at a modest stress concentration factor of 1.5.

## IV. RESULTS

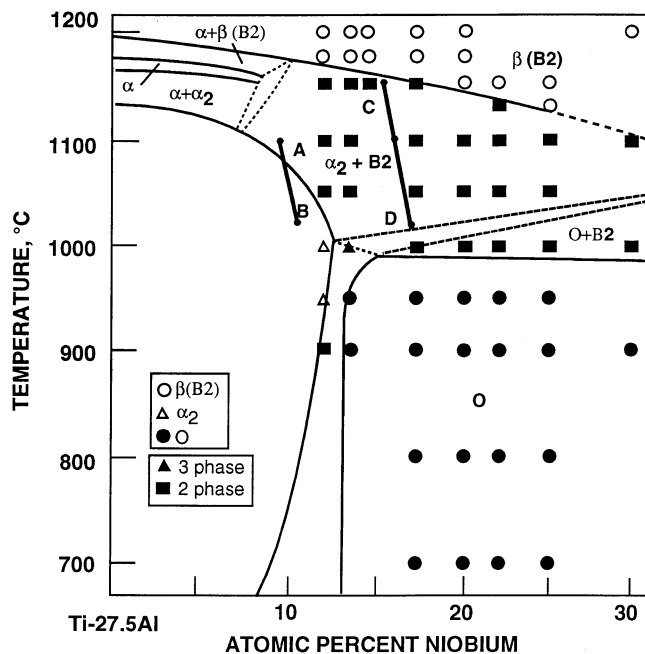
### A. Microstructures

The composition of the sheet, evaluated by chemical analysis, is provided in Table I. The  $\beta$ /B2 transus, 1150 °C, was metallographically determined by the disappearing phase method, which is based on the temperature above which the second phase (in this case the  $\alpha_2$  phase) disappears and is simultaneously accompanied by a sharp increase in the grain ( $\beta$ /B2 phase) size. A pseudobinary phase diagram for Ti-27.5Al, developed by Muraleedharan,<sup>[23]</sup> is shown in Figure 3(a) and the two-phase  $\alpha_2$  + B2 field boundaries for the current sheet material (with only 23 at. pct Al), determined by 200-hour solution treatments, are superimposed on it by the lines AB and CD. It is important to realize that such a pseudobinary does not capture the fact that the Al contents of the  $\alpha_2$  and B2 phases were different. Figure 3(a) shows that the two-phase window is significantly narrowed for the current lower Al-content alloy, as compared with Ti-27.5Al-xNb. A preliminary estimate of the Ti-22Al isopleth is reproduced in Figure 3(b) from Reference 24.

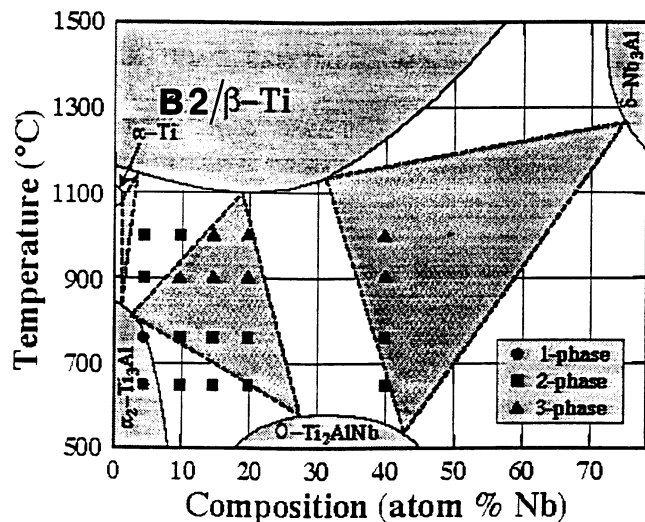
Figure 4 illustrates the as-processed and heat-treated sheet microstructures. In these backscattered photographs, the white, black, and gray regions correspond to the B2-,  $\alpha_2$ -, and O-phase regions, respectively. In the as-processed condition, Figure 4(a) shows  $\alpha_2$  (marked 1) and B2 (marked 2) grains elongated in the direction of final rolling (termed the longitudinal rolling direction (RD)). Note that  $\alpha_2$  appears to be the continuous phase. The O phase was not detected in this condition, likely because of the reasonably rapid cooling through the O-phase field from the rolling temperature. Subtransus treatments of the rolled material, followed by slow cooling to 850 °C and then aging, resulted in equiaxed  $\alpha_2$  grains and elongated O laths that grew in the prior-B2 grains. Figure 4 also compares microstructures corresponding to solutionizing temperatures of 1050 °C and 1125 °C, respectively, and illustrates significant reduction of the  $\alpha_2$  phase and  $\alpha_2/\alpha_2$  grain boundaries at the higher solutionizing temperature. The O phase has specific orientation relationships with the B2 phase<sup>[25]</sup> from which it nucleates;  $[110]_O/[1\bar{1}1]_{B2}$  and  $(001)_O/(011)_{B2}$ . Many of the neighboring larger O laths had the same crystallographic orientation, as revealed by TEM. Note also the similar direction of the major axis of those laths. The tendency for one O orientation to dominate in a given B2 grain may not only be because larger laths could consume smaller laths of different orientation, but also because a slow cool from the solutionizing temperature may favor grain boundary nucleation and growth-dominated behavior of one particular orientation relative to the others. It is notable that, for the

**Table I. Chemical Analysis of the Sheet and Neat Materials**

Alloy Form	Ti	Al	Nb	Fe (Wt Pct)	O (Wt Pct)	N (Wt Pct)
Sheet	bal	22.9	15.5	0.053	0.106	0.011
Neat	bal	21.9	14.0	0.078	0.161	0.014



(a)



(b)

Fig. 3—(a) Phase diagram for the ternary Ti-27.5Al-xNb system, taken from Ref. 23. The two-phase  $\alpha_2 + \text{B2}$  domain determined in the current study, through 200-hour solution treatments, is represented by the region between the curves AB and CD. (b) The Ti-22Al isopleth reproduced from Ref. 24.

quenched and aged conditions, the O variants and the major axis of laths were more randomly distributed even after aging times of 24 hours. A “rim” O phase, as first determined by Banerjee *et al.*<sup>[1]</sup> was sometimes observed on the boundaries of the  $\alpha_2$  grains, where this rim became obvious after creep tests at 650 °C.<sup>[15]</sup> This O phase also has an orientation relationship to the parent  $\alpha_2$  phase,<sup>[26]</sup>  $[100]_O // [2\bar{1}10]_{\alpha_2}$ , and  $(001)_O // (0001)_{\alpha_2}$ .

Table II lists the volume percents of the phases, which represent the average from a minimum of four images taken from different parts of the metallographic sample. A higher-temperature solution treatment, followed by aging, decreased the  $\alpha_2$  volume percent with a corresponding increase in the O-phase content. The B2 content changed

less drastically. The compositions of the  $\alpha_2$  and O phases, evaluated by microprobe analysis, remained relatively constant around Ti-24Al-11Nb and Ti-25Al-17Nb, respectively. Only the B2 phase composition fluctuated to accommodate different volume percents of the  $\alpha_2$  and O phases. A typical B2 composition was Ti-18Al-21Nb, which is enriched in Nb and depleted in Al compared to the base composition of the alloy.

The neat panel's composition is provided in Table I. Note that the carbon content was not measured for this material, but carbon contents found in similarly processed O alloys were approximately 130 weight parts per million (ppm).<sup>[27]</sup> The  $\beta/\text{B2}$  transus, determined by the disappearing-phase method, was approximately 1130 °C. The as-processed neat microstructure, sliced in the longitudinal RD, shows an elongated network of equiaxed  $\alpha_2$  grains with an average grain size of approximately 5  $\mu\text{m}$  and islands of irregularly shaped O + B2 regions (Figure 5(a)). The large volume fraction of the  $\alpha_2$  phase and the presence of many  $\alpha_2/\alpha_2$  boundaries are a consequence of the relatively low HIP temperature of 940 °C, which favors formation of recrystallized  $\alpha_2$  grains rather than B2 grains. The microstructure obtained after solutionizing at 1050 °C followed by a CC to 850 °C, then aging for 2 hours at that temperature, is illustrated in Figure 5(b). This particular heat treatment was selected for the neat material because identical heat treatments in the sheet material sharply reduced the fraction of  $\alpha_2/\alpha_2$  grain boundaries, which were principal crack nucleation sites.<sup>[13,14,15]</sup> The O-phase content increased and the  $\alpha_2$  phase decreased after the heat treatments (Table III), similar to the sheet material, and less  $\alpha_2/\alpha_2$  grain boundaries were obtained compared to the as-processed neat material. However, for identical heat treatments, the  $\alpha_2$  content was higher for the neat material than the sheet, probably due to a higher oxygen content in the neat material (Table I), because oxygen is known to stabilize the  $\alpha$  phases.<sup>[28]</sup>

A low magnification micrograph of the etched SCS-6/Ti-25Al-17Nb composite is provided in Figure 6(a). It shows good consolidation of the matrix around fibers except in areas where there are touching or near-touching fibers. The fiber volume fraction was approximately 0.32. The higher magnification micrograph, Figure 6(b), taken from a region halfway between fibers, shows that the as-processed composite matrix retained an even greater amount of  $\alpha_2$  than the as-processed neat material (Figure 5(a)). This is believed to be most likely due to interstitial carbon, also an  $\alpha$  stabilizer, pickup from the fiber coating during HIP of the MMC and subsequent heat treatment.<sup>[29]</sup> This is not unusual as interstitial carbon has been recorded up to 60  $\mu\text{m}$  away from the interface in SCS-6/Ti-6Al-4V.<sup>[30]</sup> Figure 6(c) illustrates the matrix region in the bulk after the MMC was subjected to the 1050 °C heat treatment. Comparison with Figure 6(b) shows that the heat treatment was able to substantially reduce the  $\alpha_2/\alpha_2$  boundaries in the bulk.

Figure 7(a), shows the matrix immediately around the fiber for the as-processed MMC, and illustrates that the matrix in the near-fiber region is significantly enriched in the  $\alpha_2$  phase and almost fully devoid of the B2 and O phases, similar to the  $\beta$ -depleted zones found in SCS-6/Ti-24Al-11Nb.<sup>[31,32]</sup> Such zones contain adjacent  $\alpha_2/\alpha_2$  boundaries that are potent sites for matrix cracks and that can significantly reduce MMC elongation, particularly in the trans-

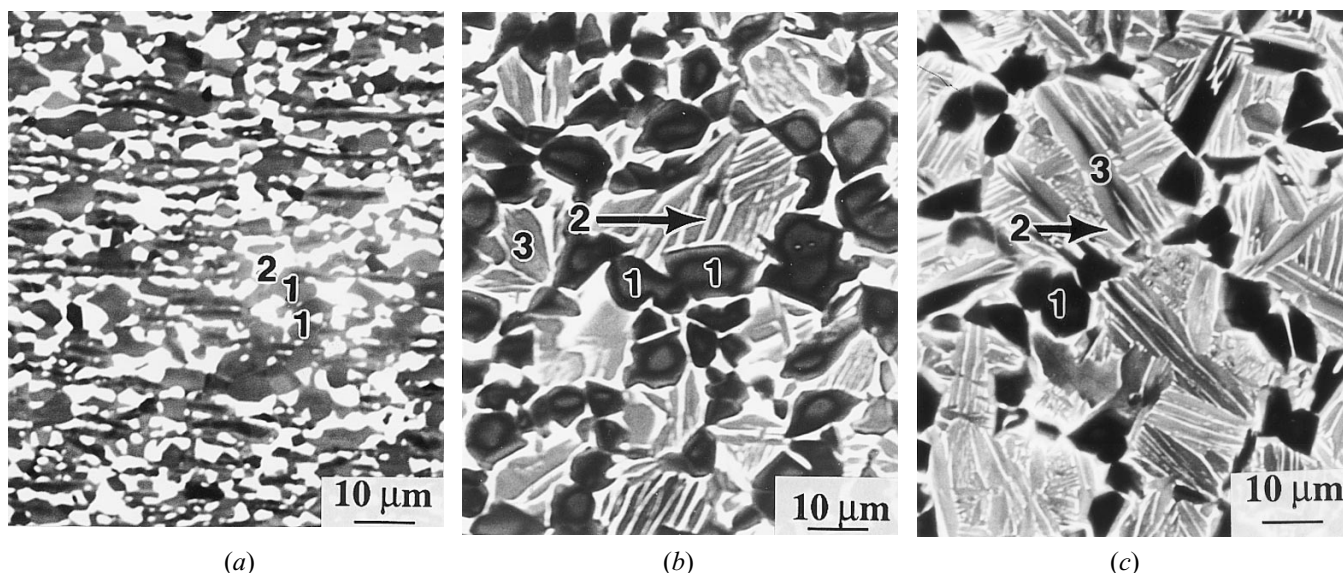


Fig. 4—Backscatter detected SEM images of the sheet material in different conditions. (a) As-rolled condition, (b) 1050 °C/1h/CC/850 °C/2h/FC, and (c) 1125 °C/1h/CC/850 °C/2h/FC. The markers 1, 2, and 3 refer to the  $\alpha_2$ , B<sub>2</sub>, and O phases, respectively.

verse (90 deg) direction. A further reduction in the B<sub>2</sub> and O contents adjacent to the fiber occurred after the heat treatment at 1050 °C. Figure 7(b) illustrates a 4- $\mu$ m-thick matrix layer fully devoid of the B<sub>2</sub> and O phases. As will be shown later, the B<sub>2</sub> phase plays an important role in imparting matrix ductility, so that  $\alpha_2$  phase stabilization due to C pickup is one of the disadvantages of using any heat treatment at all. However, far from the fibers, the  $\alpha_2$  volume percent and  $\alpha_2/\alpha_2$  grain boundaries were significantly less in the 1050 °C heat-treated condition than in the as-processed condition (Figures 6(b) and (c)). This is quantitatively illustrated in Table III, which also shows that the 1050 °C heat-treated MMC and neat materials had similar phase contents in the bulk. The  $\alpha_2$  composition in the bulk of the MMC was Ti-25Al-12Nb, identical to that for the neat.

In contrast to the uncoated fiber composite discussed previously, the single-ply MMC fabricated with Nb-coated SCS-6 fibers depicted a 2- $\mu$ m-thick O + B<sub>2</sub> phase region around the fiber (Figure 8(a)). The compositions of the different layers have been determined. The Nb-coated layer, marked Nb in Figure 8(a), had a composition of Ti-5Al-55Nb. The thin, dark layer surrounding the Nb-coated layer was rich in titanium, Ti-5Al-22Nb. The O + B<sub>2</sub> stabilized layer, marked B<sub>2</sub> + O in Figure 8(a) had a composition, Ti-17Al-32Nb, less rich in Nb than the coated layer and less rich in Ti than the dark layer. The O + B<sub>2</sub>-phase presence around the fiber is believed to be due to Nb diffusion from the coating to the matrix, which stabilizes the higher Nb-containing O and B<sub>2</sub> phases. The coating's intended purpose was to reduce the  $\alpha_2$  phase and increase the B<sub>2</sub> phase immediately around the fibers, and the microstructures showed that this was largely successful. However, the Nb layer was not of uniform thickness, likely because of uneven sputtering and uneven diffusion of Nb to the matrix during the consolidation process. This may have compromised overall transverse properties, as will be discussed later, because it is the weakest link that fails and can set up specimen failure. The fiber volume fraction was estimated to be 0.15. The B<sub>2</sub> composition in the bulk was on

the average Ti-14Al-27Nb. The  $\alpha_2$  composition, Ti-25Al-12Nb, was constant throughout the matrix and was identical to that for the neat and SCS-6/Ti-25Al-17Nb composites.

Comparing regions A and B of Figure 8(b), it is observed that the areas between the fibers had more  $\alpha_2$  phase and  $\alpha_2/\alpha_2$  boundaries compared to regions far away. Figure 8(c) taken from region B of Figure 8(b) is comparable to that for the heat-treated neat material, Figure 5(b) Phase contents are shown in Table II. On the other hand, the regions surrounding the O + B<sub>2</sub> stabilized zone, Figure 8(a) and region A of Figure 8(b) have more  $\alpha_2/\alpha_2$  boundaries compared to that of Figure 8(c) probably due to carbon diffusion.

## B. Properties

Table II lists the RT properties for all the sheet specimens. Only one test was performed for most of the heat-treated conditions, yet these results provide general microstructure-property trends. The super transus-treated material, containing an average  $\beta$ /B<sub>2</sub> grain size of 200  $\mu$ m, proved to be strong but brittle, reaching a fracture stress of 1150 MPa. However, the failure strain was only slightly above 1 pct. On the other hand, the subtransus treatment provided good ductility and lower strengths. Figure 9 indicates that the subtransus solution treatment temperature had only a small effect on the elastic modulus (E), yield strength (YS), and ultimate tensile strength (UTS) of the alloy. Strains-to-failure for such specimens ranged from 7 to 14 pct, which is excellent for MMC purposes. It is shown in References 13, 14, and 15 that, although the subtransus treatments produced similar RT tensile stress-strain curves, higher solutionizing temperatures produced significant improvements in creep and fatigue crack growth resistance. Thus, there indeed is a benefit in going to microstructures with lower  $\alpha_2$  contents.

The tensile properties of the neat and [O]<sub>4</sub> composites are provided in Table III. The data represent the average of at least two specimens per condition, with the only exception

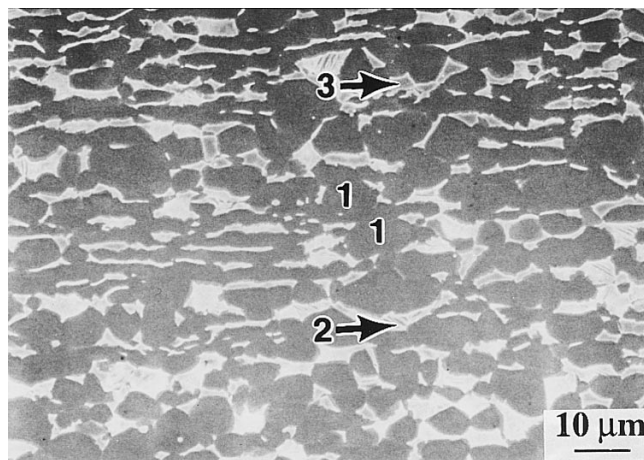
**Table II. Heat Treatments and Room-Temperature Properties for Ti-25Al-17Nb Sheet Material**

Heat Treatment	Volume Percent			0.2 Pct YS (MPa)	UTS (MPa)	Strain (Pct)
	$\alpha_2$	B2	O			
<b>Longitudinal</b>						
<b>Supertransus treatments</b>						
1190 °C/.25 h/AQ	—	—	—	—	1154	1.2
<b>Subtransus treatments</b>						
As-rolled	64.1	35.9	0.0*	681	775	10.7
925 °C/24 h/FC	76.4	23.6	0.0*	617	840	12.3
1050 °C/1 h/WQ/850 °C/2 h/WQ	57.5	23.9	18.6	691	906	14.0
1050 °C/1 h/CC/850 °C/2 h/FC	53.4	25.8	20.8	564	805	10.7
1075 °C/1 h/CC/850 °C/24 h/FC	43.3	13.0	43.7	587	780	9.5
1100 °C/1 h/CC/850 °C/2 h/FC	17.9	19.7	61.8	569	748	7.0
1125 °C/1 h/CC/850 °C/2 h/FC	17.1	18.9	64.0	547**	785**	10.2**

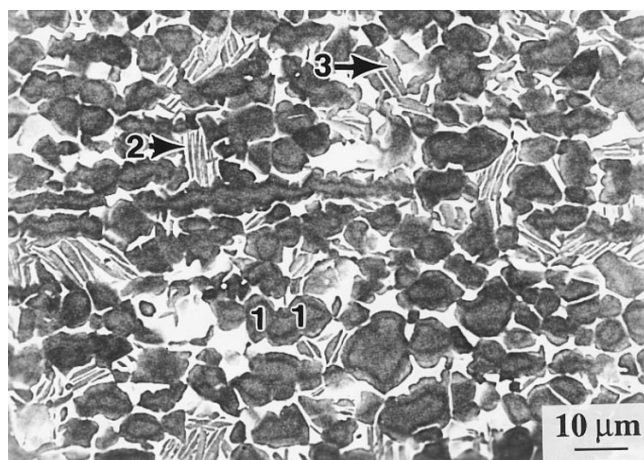
AQ: air quenched; FC: furnace cooled; WQ: water quenched; —: undetermined; and CC: control cooled at 28 °C/min.

\*Some O phase may be present.

\*\*Averaged values.



(a)



(b)

Fig. 5—Microstructures of the neat material. (a) As-processed condition and (b) heat treated at 1050 °C. The markers 1, 2, and 3 refer to the  $\alpha_2$ , B2, and O phases, respectively. Note that the heat-treated microstructure contains less  $\alpha_2/\alpha_2$  grain boundaries and more O phase.

being for the single-ply 90 deg MMC, where only one test was performed. Heat treatment of the neat specimens drastically increased the strain-to-failure (greater than 3 times), although the flow stress decreased modestly (Figure 10). In

the case of the  $[0]_4$  MMC, heat treatment significantly improved both the strain-to-failure and UTS. The stress-strain curves for the MMCs, (Figure 11) exhibited an initial elastic deformation of the fibers and plastic deformation of the matrix. Transverse strain measurements showed increase in the Poisson's ratio after the bend in the stress-strain curve, indicative of plasticity of the matrix. However, the plasticity stage was shortened for the as-processed condition compared with the heat-treated condition, indicative that large-scale failure of fibers occurred earlier for the former. If fiber degradation due to heat treatment was an issue by itself, then one would anticipate lower strength after the heat treatment due to reaction with the matrix. Clearly an alternate mechanism is operative.

Similar to other titanium aluminide composite systems, the moduli data contained a wide amount of scatter. The 12 pct decrease in modulus for the heat-treated  $[0]_4$  composite compared to the as-processed condition can be partly explained using the isostrain equation:

$$E_c = E_f v_f + E_m (1 - v_f) \quad [11]$$

where  $E_c$ ,  $E_f$ , and  $E_m$  are the elastic moduli of the composite, fiber, and matrix, respectively. The as-processed modulus (97 GPa) for the neat material was greater than that of the heat-treated neat (88 GPa) material, which can be explained in terms of the higher O-phase content of the latter material. Elastic modulus data on O alloys show that the O phase is the most compliant of the three phases.<sup>[33]</sup> Using a fiber volume fraction of 0.32 and the measured fiber modulus of 376 GPa for the heat-treated composite fibers, we obtain  $E_c = 180$  for the heat-treated  $[0]_4$  composite and  $E_c = 187$  for the as-processed condition. Both these values are within 6 pct of the measured data (Table III).

In comparison to the  $[0]_4$  MMC, Figure 12 shows that heat treatment did not produce as significant an improvement in the strength and strain-to-failure of the  $[90]_4$  MMC. It is well known that fiber-matrix debonding under transverse loading can set up high stress concentration around the fibers. Such stresses can initiate matrix cracks, which can rapidly grow to failure if the fracture toughness of the matrix is low. When the matrix possesses sufficient toughness, as in the case of SCS-6/Ti-15V-3Cr-3Al-3Sn MMCs,



**Table III. Heat Treatments and RT Tensile Properties for Ti-25Al-17Nb Neat Material and SCS-6/Ti-25Al-17Nb Composites**

Heat Treatment	Volume Percent			0.2 Pct YS (MPa)	UTS (MPa)	Strain (Pct)	<i>E</i> (GPa)
	α <sub>2</sub>	B2	O				
<b>Neat</b>							
As-processed	74.8	16.3	8.9	781	801	1.09	97.3
1050 °C/1 h/CC/850 °C/2 h/FC	64.1	19.2	16.7	670	759	4.00	88.2
<b>[0]<sub>4</sub> SCS-6/Ti-25Al-17Nb</b>							
As-processed	80.0	11.5	8.5	—	1367	0.86	192.6
1050 °C/1 h/CC/850 °C/2 h/FC	68.5	12.0	19.5	—	1579	1.15	170.3
<b>[90]<sub>4</sub> SCS-6/Ti-25Al-17Nb</b>							
As-processed	80.0	11.5	8.5	—	256	0.20	145.0
1050 °C/1 h/CC/850 °C/2 h/FC	68.5	12.0	19.5	—	250	0.23	114.2
<b>[90] NbSCS-6/Ti-25Al-17Nb</b>							
As-processed	53.3	15.6	31.1	—	397*	0.40*	118*

CC: control cooled at 28 °C/min; FC: furnace cooled; and — undetermined.

\*Represents only one test per condition.

RT strain-to-failures of about 1.4 pct are observed.<sup>[34]</sup> On the other hand, titanium aluminide-based MMCs have shown 90-deg ductilities ranging from 0.2 to 0.5 pct, resulting mainly from low toughness of the material.<sup>[9]</sup> The data in Table III show that the SCS-6/Ti-25Al-17Nb system is no exception. Of relevance is the fact that the fracture toughness of the sheet material in the 1050 °C treated condition was approximately 22 MPa√m.<sup>[15]</sup> Added to this relatively low toughness value was the significant depletion of B2 phase and enrichment of  $\alpha_2$  immediately surrounding the fiber. The single-ply [90] specimens with Nb-coated fibers, however, showed an improvement of both UTS and strain-to-failure. Figure 12 shows a strength improvement of approximately 60 pct and an elongation improvement of about 100 pct compared with the uncoated-fiber composites. Additionally, whereas the uncoated-fiber composites failed almost at the onset of nonlinearity, the Nb-coated fiber specimen showed modest strain accumulation past that point.

### C. Deformation Behavior and Fractography

#### 1. Slip

The slip behavior of the sheet material has been well documented in previous studies<sup>[13,14,15]</sup> and will only be summarized here. The SEM images (Figure 13) depict slip in each of the constituent phases. Slip bands were observed to be planar in the  $\alpha_2$  and O grains (Figures 13(a) and (c), respectively). In contrast, slip in the B2 region was wavy (Figure 13(b)). Slip compatibility existed between the O and B2 phases, arising from the favorable orientation relationship between the O-phase laths and the parent B2 phase.<sup>[25]</sup> Slip was observed to pass directly from O to B2 back to O without deflection (Figure 14) or jogged at B2 boundaries (Figure 13(c)). Preliminary TEM analysis of the O phase in a deformed sheet specimen showed both  $\langle a \rangle$  and  $\langle c + a \rangle$  dislocations, with the  $\langle a \rangle$  type ( $\langle 100 \rangle$  and  $\langle 110 \rangle$ ) dislocations dominating over  $\langle c + a \rangle$  ( $\langle 114 \rangle$ ) dislocations. The TEM studies also showed that O slip bands were jogged at the B2 boundaries, and sometimes they transgressed straight through the boundaries.

#### 2. Cracking

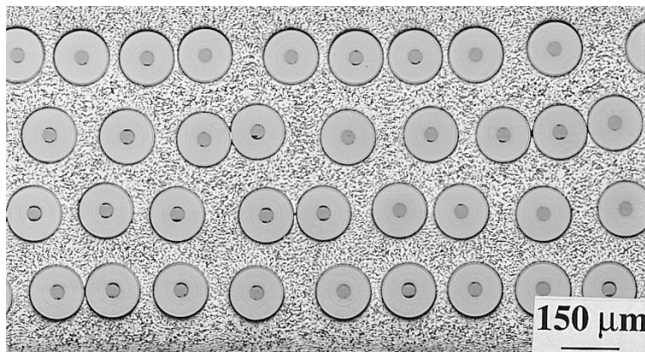
The subtransus-treated sheet exhibited a mixture of cleavage fracture of  $\alpha_2$  grains, faceted fracture of O laths,

and dimple fracture of the retained B2 phase. These are illustrated in Figure 15. Both the ductile fracture morphology of the B2 phase and its ability to blunt cracks (Figure 13(a)) illustrate its very important role in imparting ductility and fracture resistance to the alloy. Although O-phase fracture is faceted, suggestive of limited ductility, it has better straining capacity than the  $\alpha_2$  phase, which fails by cleavage. More importantly, the O phase imparts creep resistance to the alloy, which is critical for high-temperature applications.<sup>[15]</sup>

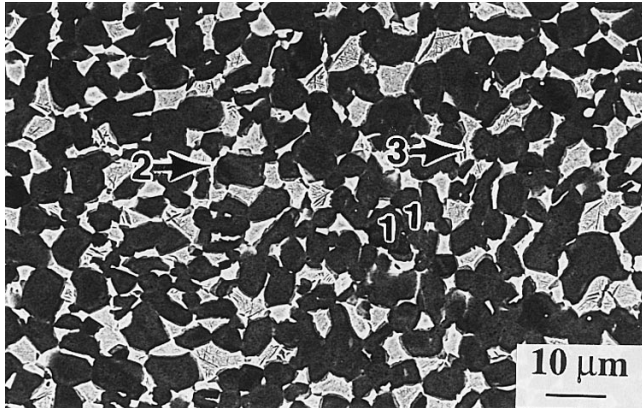
An important mode of cracking of the alloys was  $\alpha_2/\alpha_2$  grain boundary cracks. Figures 13(a) and 16(a) illustrate this for the sheet material. This mode was dominant for the as-processed neat and composite materials, and it is believed to be largely responsible for the poor matrix ductility. For the sheet material, a solutionizing temperature of 1125 °C was able to remove most adjacent  $\alpha_2/\alpha_2$  grain boundaries and, thus, most of this cracking mode. The problem with applying the same heat treatment to the MMC was the stabilization of  $\alpha_2$  phase caused by carbon diffusion from the fiber,<sup>[29]</sup> thus preventing elimination of such boundaries. A more modest temperature of 1050 °C was, therefore, selected for the MMC in an effort to reduce carbon intake by the matrix. However, at this temperature, some adjacent  $\alpha_2/\alpha_2$  boundaries were retained. Figure 16(b) shows such cracks near the fracture plane of a 1050 °C treated neat material. In the as-processed condition, there were many more such cracks throughout the gage length of the sample rather than being concentrated near the fracture plane. In the MMC as well, the incidence of grain boundary cracks in the 1050 °C treated material was significantly less than for the as-processed condition.

The fracture surfaces of the as-processed and heat-treated MMCs exhibited matrix failure behavior similar to that of the neat and sheet specimens. However, the fracture surface was significantly rougher for the heat-treated MMC compared to the as-processed MMC. The matrices of both types of specimens were etched out to reveal the incidence of fiber fractures in the samples. If fractures within a 1-mm distance from the fracture surface are neglected (to avoid dynamic load-induced failures), both the as-processed and heat-treated MMCs showed extremely few fractures: a maximum of 6 to 8 fiber breaks in each sample out of a total of about 145 fibers per sample. Figure 17 is a low-magni-

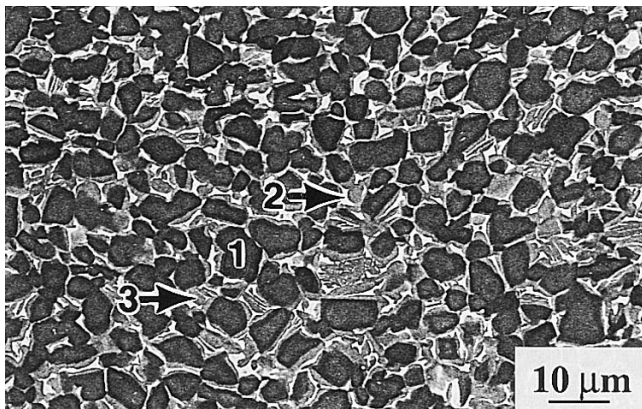




(a)



(b)

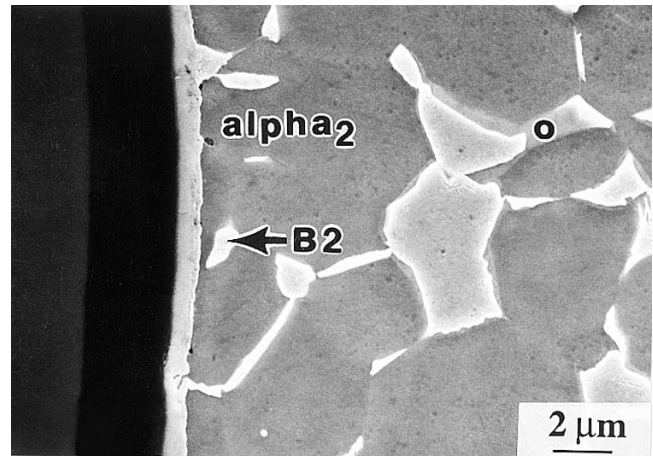


(c)

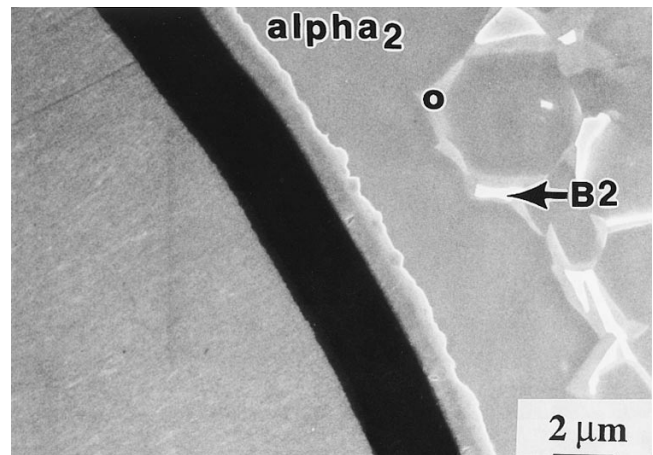
Fig. 6—(a) Low-magnification micrograph of the as-processed composite. (b) and (c) correspond to the as-processed and heat-treated  $[0]_4$  composite, respectively, and correspond to locations away from the fibers. Note that the heat-treated composite matrix contains less  $\alpha_2/\alpha_2$  grain boundaries and more O phase in the bulk.

fication micrograph where the matrix has been etched out to reveal the fibers. No fiber fractures are seen here. On the other hand, polished sections showed multiple fiber fractures within 1- to 2-mm distance from the fracture plane, similar to what has been observed in other studies.<sup>[31,34]</sup> Clearly, fiber fractures are not randomly distributed but are extremely localized around the fracture plane. This is contrary to expectations based on global load-sharing behavior. We shall return to this subject later in Section V.

For the  $[90]_4$  composites, debonding occurred primarily at the interface between the reaction zone and the SCS coat-



(a)

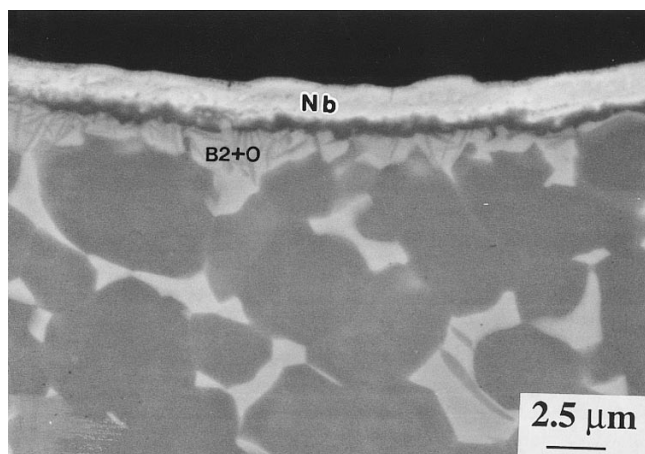


(b)

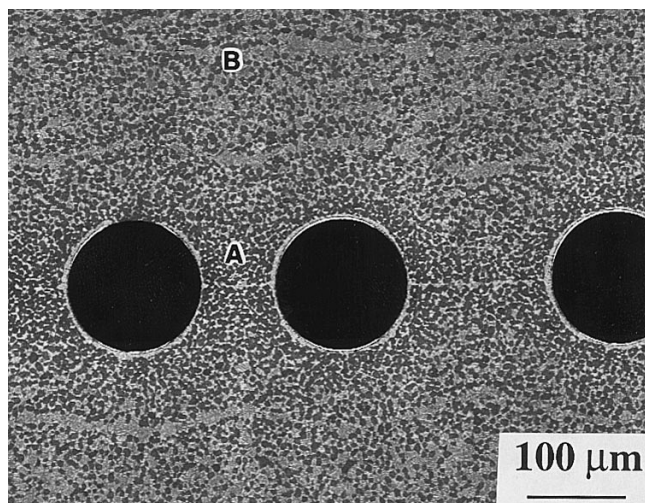
Fig. 7—The fiber-matrix interface region for the (a) as-processed and (b) heat-treated composite.

ing. In addition to the main crack, many radial matrix cracks perpendicular to the loading direction were observed immediately around the fibers. The high local stress and accompanying fiber-matrix debonding, together with the less ductile  $\alpha_2$  enriched zone, are believed to be largely responsible for such cracking in both the as-processed and heat-treated MMCs. This may explain why heat treatment of the  $[90]_4$  MMC was unable to impart any significant improvement on the strength and elongation.

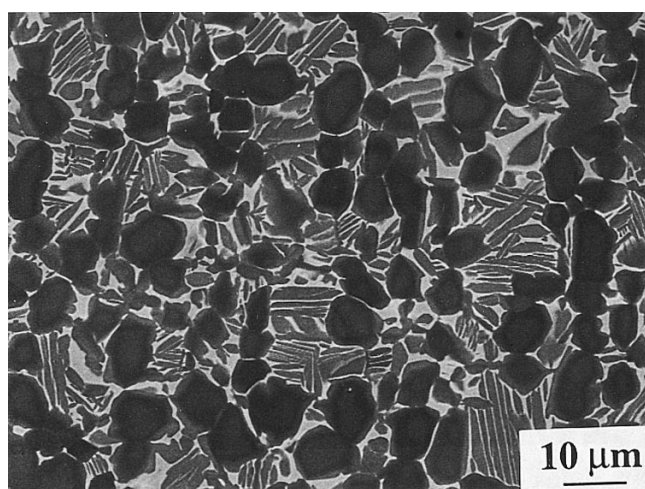
The single-ply  $[90]$  specimen with the Nb-coated fibers exhibited a different behavior. Figure 18(a) shows a region near the fracture plane (the loading axis is horizontal), where some  $\alpha_2$  enrichment may be observed outside the O + B2 stabilized region around the fiber. Radial cracks initiated around the fiber, similar to other 90-deg samples. However, in many places it appeared that radial cracks originated in the outer  $\alpha_2$  enriched zone rather than from the fiber-matrix interface. Figure 18(b) is a higher magnification micrograph of region A of Figure 18(a). A crack is pointed out by the longer arrow. Note that the crack opening is larger in the  $\alpha_2$  phase than in the O + B2 region. If cracking had initiated in the Nb-rich layer, then its opening should have been larger than in the  $\alpha_2$  phase. The smaller arrow in Figure 18(b) points to another crack that also has initiated in the outer  $\alpha_2$  region but has been pre-



(a)



(b)



(c)

Fig. 8—Micrographs of the single-ply Nb-coated SCS-6/Ti-25Al-17Nb composite depicting (a) the O + B2 stabilized zone and (b) the  $\alpha_2$  stabilized region (A) between the fibers. (c) Bulk matrix microstructure corresponding to region B of (b).

vented from reaching the fiber by the O + B2 layer. Thus, addition of the Nb layer does indeed appear to help delay the onset of radial cracking from the fiber-matrix interface

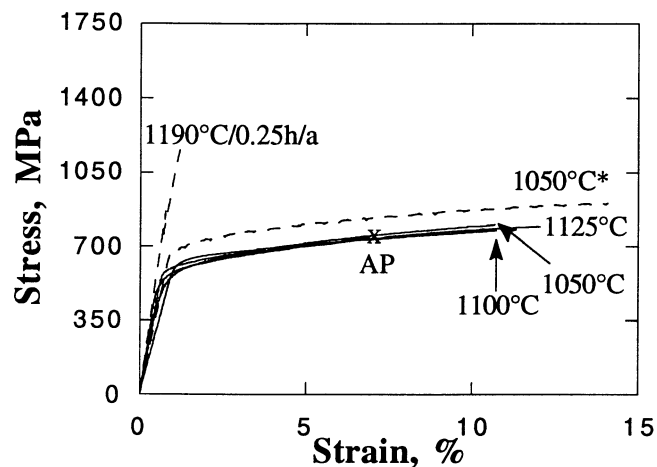


Fig. 9—Stress-strain curves for the as-processed (AP) and heat-treated sheet material. The solution treatment temperatures are indicated. All heat-treated specimens were CC, then aged at 850 °C, except the one indicated by an asterisk; this latter specimen was quenched rather than control cooled after solutionizing.

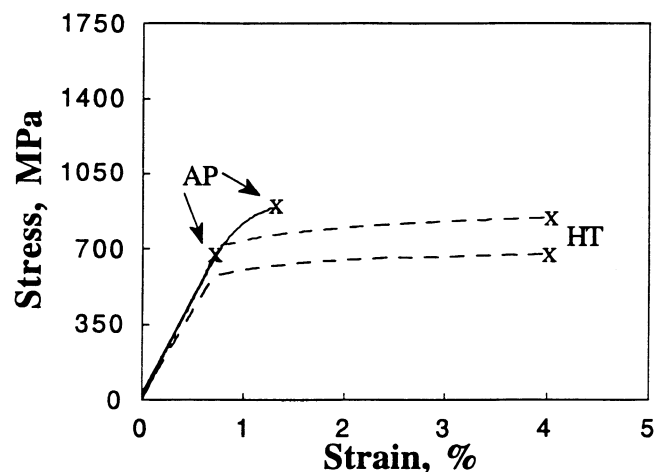


Fig. 10—Stress-strain curves for the as-processed (AP) and heat-treated (HT) neat material. Note the significant improvement in the strain-to-failure after the heat treatment.

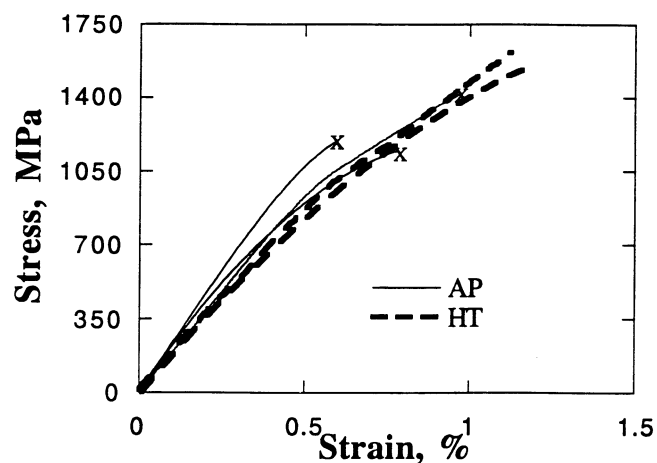


Fig. 11—Stress-strain curves for the as-processed (AP) and heat-treated (HT) SCS-6/Ti-25Al-17Nb [0]<sub>s</sub> specimens.

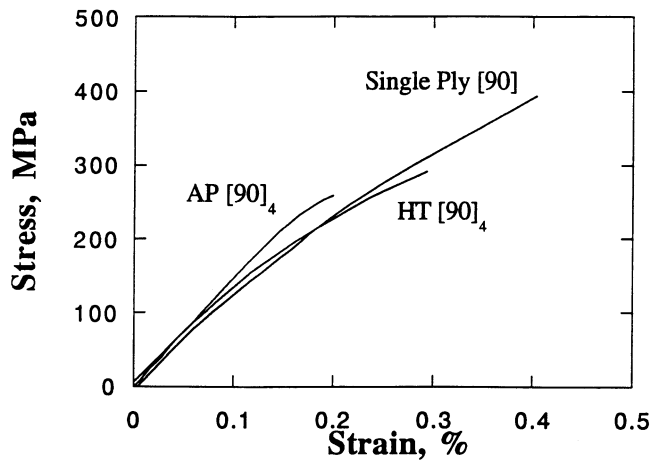
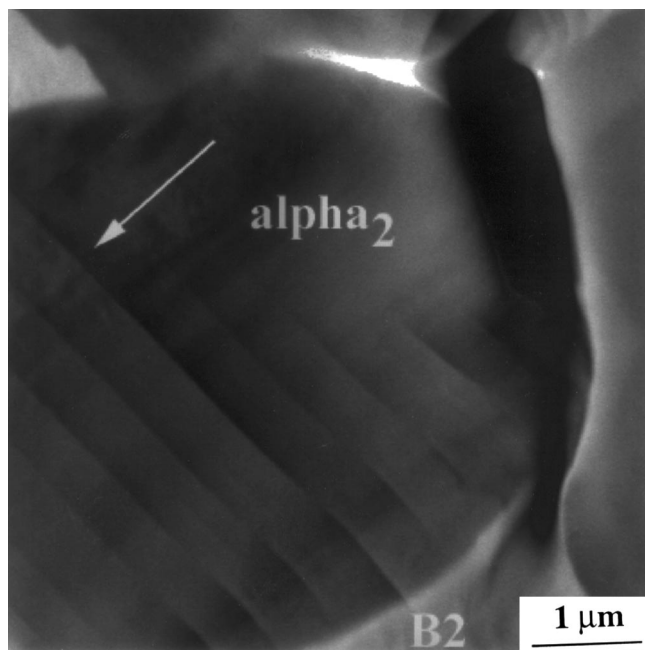
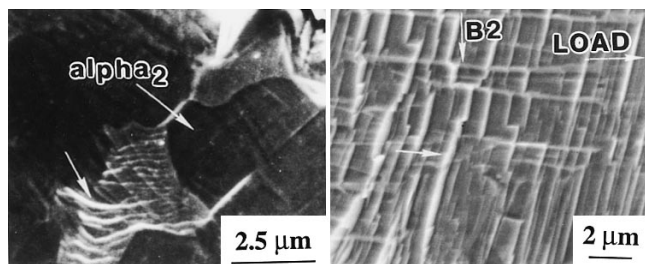


Fig. 12—Stress-strain curves for  $[90]_x$  specimens.



(a)



(b)

(c)

Fig. 13—Microstructures of the matrix showing slip traces (see unlabeled arrows) in the different phases. (a) Planar slip in the  $\alpha_2$  phase. An  $\alpha_2/\alpha_2$  grain boundary crack that was blunted by the B2 phase can also be seen in this figure. (b) Wavy slip in the B2 phase. (c) Planar slip traces in the O laths that are jogged by the retained B2 phase; the B2 strips are horizontal, while the slip traces are approximately 10 deg from the vertical axis.

with a consequent improvement in MMC elongation (Figure 12). However, the photomicrographs show that the outer  $\alpha_2$  enrichment must be avoided.

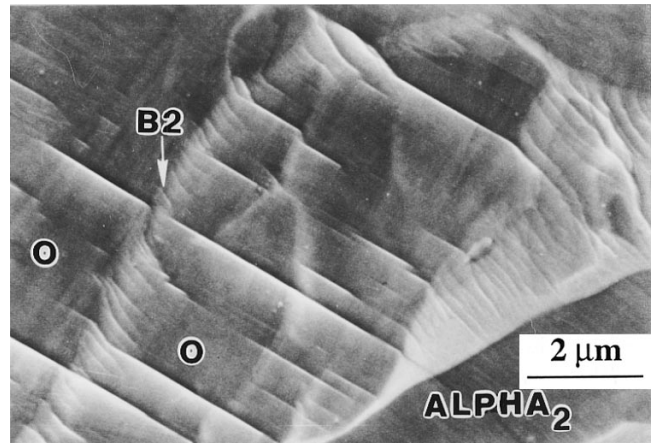


Fig. 14—Slip transmission from the O to the B2 phase; note planar slip in the O phase and wavy slip in the B2 phase.

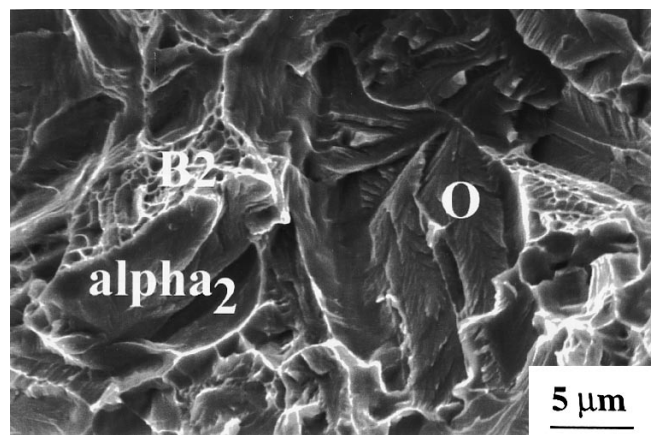
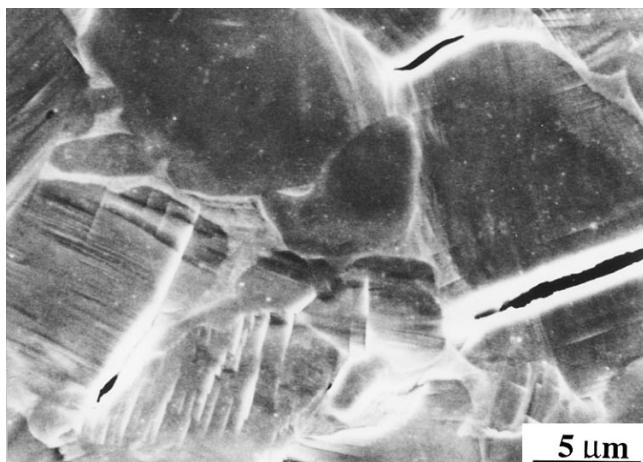


Fig. 15—Fracture surface of the sheet material exhibiting a cleaved  $\alpha_2$  grain, faceted fracture of the O phase, and ductile dimpling of the B2 phase.

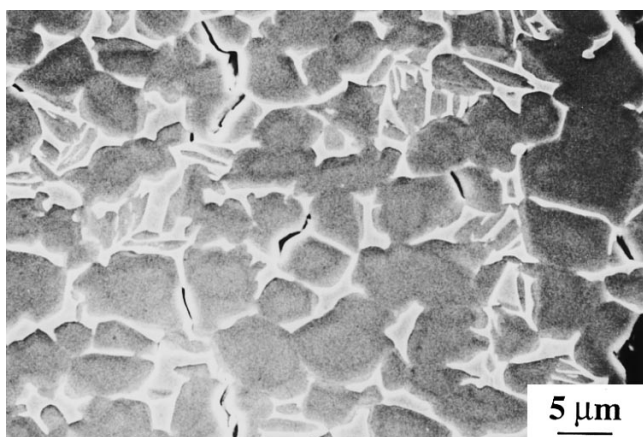
## V. DISCUSSION

The matrix microstructure of a SCS-6/Ti-25Al-17Nb alloy was modified by heat treatment in an effort to improve the RT tensile properties in both the 0- and 90-deg directions. As part of the approach, the structure-property relations for the sheet and neat materials were studied to guide selection of an appropriate microstructure for the composite.

A wide variation of microstructures was obtained for the sheet material using different heat treatments. Solutionizing in the two-phase  $\alpha_2 + \text{B2}$  field, followed by aging in the O-phase region, provided elongations greater than 7 pct. Among the three phases, the B2 phase appears to play a pivotal role in imparting ductility and toughness to the alloy. Slip band observations showed wavy slip character for this phase, and fracture surfaces revealed ductile dimple fracture. In contrast,  $\alpha_2$  slip was planar, and incompatibility stresses at grain boundaries helped to open up  $\alpha_2/\alpha_2$  cracks. Such cracks were largely responsible for the poor ductility of the as-processed neat material. On the other hand, when such boundaries were reduced, as in the 1050 °C treated neat material, the elongation increased to 4 pct. It is not clear whether such an elongation is sufficient to utilize the full strength capability of fibers, because large strain con-



(a)



(b)

Fig. 16— $\alpha_2/\alpha_2$  grain boundary cracking in heat-treated specimens: (a) sheet material and (b) neat material.

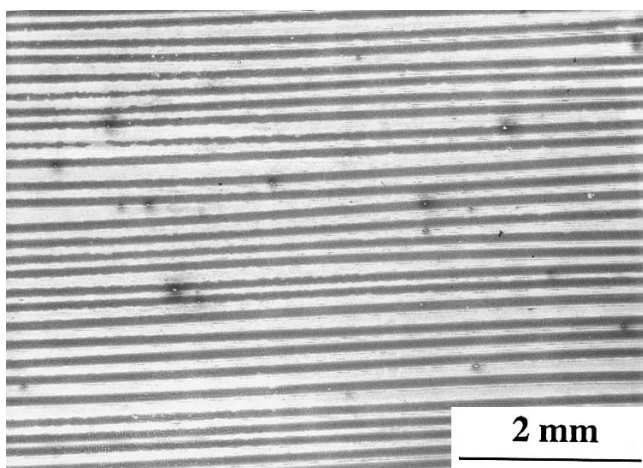
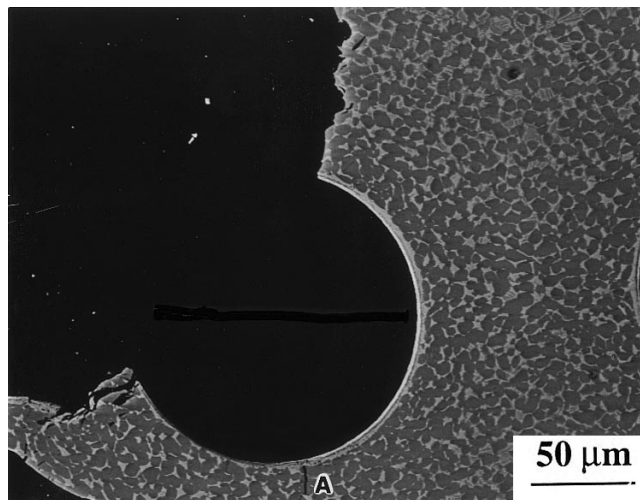
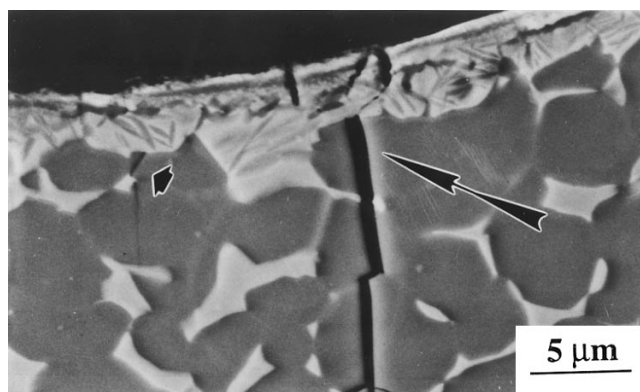


Fig. 17—Low-magnification SEM image of the tested heat-treated  $[0]_4$  specimen after the matrix was removed by etching. No fiber fractures can be observed.

centrations occur immediately adjacent to fiber breaks. However, considering that even larger elongations most likely will be accompanied with decreases in creep resistance, a value of 4 pct may be considered as a reasonable value.



(a)



(b)

Fig. 18—Cracking in the single-ply 90-deg Nb-coated SCS-6/Ti-25Al-17Nb MMC. (a) Low magnification micrograph. (b) Higher magnification micrograph of the region surrounding the fiber, which is located at the top left of the picture, illustrating preferential cracking in the  $\alpha_2$  enriched zone.

The O slip was also planar. However, there were little, if any, O cracks, in contrast to the  $\alpha_2$  phase, which also deformed by planar slip. One reason for the better performance of the O phase (aside from its superior creep resistance<sup>[35]</sup>) is the existence of  $\langle c + a \rangle$  slip. Such slip is principally absent in the  $\alpha_2$  phase at all temperatures. Another important reason for no cracking in the O laths was the intervening B2 phase between the O laths. The B2 phase helped to prevent stress concentrations that build up when planar slip extends over large distances. Figure 13(c) showed that O slip was jogged at B2 boundaries, thereby reducing stress buildup in the O phase.

The experiments do show that careful attention needs to be focused on the alloy composition and interstitial content in selection of heat-treatment conditions. Thus, in the 1050 °C treated condition, the elongation of the neat material was significantly less than that for the sheet. The higher oxygen content of the neat may have contributed directly to lower elongation through  $\alpha_2$  stabilization, although defects (particularly in the  $\alpha_2$  phase) caused by cold rolling used for foil manufacture cannot be ruled out.

In the case of the MMC, the diffusion of carbon from the fiber coating poses a significant problem in selecting a

**Table IV. Predicted Fiber and MMC Stresses at Failure of 0-Deg MMCs, Using Different Models and Fiber Data from Current and Previous Work (Predicted MMC Strengths May Be Compared with the Measured Strengths Listed at the Bottom of the Table)**

<b>Base Data for SCS-6 Fibers</b>				
Fiber Data Reference	$\sigma_0$ (MPa)	$m$	$L_0$ (mm)	
Current study	4017	13.0	25.4	
Ref. 37	4510	10.5	25.4	
Ref. 31 (lower strength fibers)	3851	17	12.7	
<b>Predictions for Fiber Stress at MMC Failure</b>				
Fiber Data Reference	$\sigma_{\text{dbf}}$ dry bundle (MPa)	$\sigma_{\text{glf}}$ Curtin <sup>[17]</sup> (MPa)	$\sigma_{\text{fbf}}$ first break (MPa)	$\sigma_{\text{sfb}}$ second break, Zweben and Rosen <sup>[18]</sup> (MPa)
Current study	3041	3616	2855	3311
Ref. 37	3263	3993	2957	3625
Ref. 31	2942	3376	2849	3132
<b>Predictions of MMC Strength</b>				
Fiber Data Reference	$\sigma_{\text{MMC}}$ dry bundle (MPa)	$\sigma_{\text{MMC}}$ Curtin <sup>[17]</sup> (MPa)	$\sigma_{\text{MMC}}$ first break (MPa)	$\sigma_{\text{MMC}}$ second break, Zweben and Rosen <sup>[18]</sup> (MPa)
Current study	1483	1667	1424	1570
Ref. 37	1554	1788	1456	1670
Ref. 31	1451	1590	1422	1512

Measured MMC strengths were **1367 MPa** and **1579 MPa** for the as-processed and heat-treated MMCs, respectively.

suitable heat treatment.<sup>[29]</sup> Among the sheet, neat, and MMC materials, the matrix of the MMC had the highest  $\alpha_2$  content after the same heat treatment. This is likely due to the presumed increased level of carbon picked up by the matrix from the fiber coating. A possible solution is a higher heat-treatment temperature to get the desired microstructure. However, a problem with this is that carbon intake by the matrix would also increase, resulting in retention of significant amounts of  $\alpha_2/\alpha_2$  boundaries in the bulk and a larger  $\alpha_2$  enriched zone around the fiber. The alternate approach of Nb-coated fibers did offer promise of improved toughness around the fiber through retention of the O and B2 phases, and modest improvements in strength and elongation of the 90-deg MMC were obtained. However, more attention needs to be focused on obtaining defect-free, uniform coatings. Also, steps have to be taken to prevent large-scale diffusion of carbon into the matrix.

It is generally believed that the matrix plays only a minor role in 0-deg MMC strength, with its quantitative effect being realized by the second term of Eq. [1]. Thus, assuming that the matrix is yielded and the flow stress does not change with the microstructure, one would anticipate no significant gains in MMC strength. This is contrary to the results and emphasizes the fact that the matrix condition also influences the strength utilization of the fiber. Further considerations on this issue are discussed later.

Using the equations in Section III and fiber strengths obtained from the current work, the tensile strengths of the 0-deg MMC were computed (Table IV). Additional parameters used in the calculations were a friction stress of 50 MPa<sup>[31]</sup> for the Curtin model (this provides a lower bound estimate of strength based on that particular model, although a friction stress of approximately 150 to 300 MPa is more appropriate based on fragmentation tests<sup>[36]</sup>), a gage length of 26.7 mm for the MMC tensile coupons, and a

total of 145 fibers in the gage section (4 plies 8 mm in width with a fiber volume fraction of 0.32). The value of  $\sigma_{um}$  was equated to the flow stress of the neat material which, based on the stress-strain curves of the neat material (Figure 10), was taken to be 750 MPa for both the as-processed and heat-treated microstructures. Fiber strength data from SCS-6/Ti-22Al-23Nb<sup>[37]</sup> and SCS-6/Ti-24Al-11Nb<sup>[31]</sup> MMCs, and MMC strength predictions based on them, are also included in Table IV for comparison purposes. The predicted strengths in Table IV have to be compared with measured tensile strengths of 1367 and 1579 MPa for the as-processed and heat-treated MMCs, respectively. In this table, the strengths based on the dry bundle strength are believed to be less relevant, because friction stresses are quite high at RT. Therefore, the discussion will focus on the other three models.

Table IV shows that the measured tensile strength of the as-processed MMC is only comparable to the predicted strength based on the occurrence of the first fiber fracture. This is consistent with the fact that the matrix of the as-processed MMC had a poor ductility (Table III). As already indicated in the modeling section, when the first fiber break to cause nucleation and propagation of a matrix crack. Further evidences of a matrix-dominated failure (after nucleation from a fiber break) were the very few dispersed fiber breaks (6 to 8) and the fact that the fracture surface was flat and smooth with very small fiber pull-out lengths (maximum of 1 fiber diameter). All these evidences tend to suggest that the first fiber fracture criteria may be a good one for this system and for other systems with very low ductility matrices. In this context, it is also useful to point out that, when this criteria was used to predict the strength of a SCS-6/Ti-24Al-11Nb MMC,<sup>[31]</sup> where the matrix also had low ductility, a good correlation was obtained. Thus, for the MMC with 100 pct “strong” fibers, a strength of 1417



MPa was predicted, compared with a measured strength of 1465 MPa.<sup>[31]</sup> Correspondingly, for the MMCs with 100 pct "weak" fibers, the predicted strength was 1224 MPa, compared with a measured strength of 1160 MPa.<sup>[31]</sup> These predicted strengths were more than 150 MPa below what was calculated with the Curtin model.<sup>[16]</sup> While distributed fiber cracks were metallographically observed for their system, it is possible that mechanical polishing of specimens with a residual tensile stress in the fibers (after tensile fracture) can result in formation of distributed fiber cracks.<sup>[38]</sup> Overall, these results suggest that in low-ductility matrices, MMC strength is well represented by a failure criterion based on the first fiber break.

In the case of the heat-treated MMC, the averaged measured strength was significantly above the stress predicted by the first fiber fracture. Thus, consistent with the higher ductility of the heat-treated neat material, the first fiber fracture is unable to propagate a matrix crack through the MMC. Table III shows that the measured strength of 1579 MPa was much lower than the MMC strength based on Curtin's global load-sharing model<sup>[16]</sup> using the current fiber data. Additional confirmation on the absence of global load sharing was that etched-out fibers indicated less than 8 fiber breaks away from the fracture surface, whereas more than 100 random fiber breaks were predicted by the Curtin model. Thus, these evidences suggest local, rather than global, load sharing, and likely reasons include stress concentrations through elastic<sup>[22]</sup> and plastic<sup>[20,21]</sup> effects.

Table IV shows strengths predicted by the second-fiber-fracture model. This model emphasizes local load-sharing behavior through stress concentration in a fiber adjacent to a broken fiber. The strength based on this model is 1570 MPa, which is extremely close to the averaged measured value. While this does not by itself confirm the applicability of the model based on the second fiber fracture, the observed absence of fiber fractures away from the crack plane suggests that this may be a likely one for the heat-treated MMC. The predicted strain-to-failure, using the measured fiber data and a calculated residual fiber stress of -621 MPa (using a concentric cylinder analysis), was 1.05 pct, which is in excellent agreement with the averaged measured strain of 1.15 pct. It was already indicated that the second-fiber-fracture model was found to provide good predictions of strength for boron-aluminum MMCs over a wide range of fiber volume fractions.<sup>[17]</sup>

It may be noted that, while a sufficient knowledge base exists about deformation mechanisms up to the point of instability in MMCs, it is not at all clear as to what occurs right at the point of instability. The current comparisons of the predicted and measured strengths do provide useful information about conditions existing at the onset of MMC failure and how the matrix microstructure influences that onset. Thus, in the as-processed condition, final failure is likely to have been triggered by the formation of a fiber break at a high enough stress such that the local stress intensity factor was higher than the fracture toughness of the matrix material. For the heat-treated MMC, the strength data suggest that failure was not triggered by this mechanism because of higher toughness and ductility of the matrix, but that local stress concentration likely played a role. The analysis also shows that by suitably improving the matrix microstructure, the fibers in MMCs would be more ef-

ficiently utilized. The maximum utilization would be under global load-sharing conditions.

## VI. SUMMARY

The results show that significant improvements can be obtained in the RT tensile strength of MMCs by modifying the matrix microstructure through heat treatments. The roles of the matrix are twofold: (1) for the 0-deg MMC, it provides more efficient utilization of the strength characteristics of the fibers; and (2) for the 90-deg MMC, it can offer resistance to the nucleation and growth of a matrix crack in the highly stressed region around the fiber after fiber-matrix debonding.

A number of fiber strength models were assessed to determine their applicability to the RT strength of the 0-deg SCS-6/Ti-25Al-17Nb MMC. While a fiber strength model corresponding to the onset of the first fiber fracture provided good correlation with the strength of the as-processed MMC, the model based on the second fiber fracture appeared to be attractive for the heat-treated MMC. These correlations were in agreement with the ductility of the matrix material with differing microstructures. Additional evidence for the applicability of the two models was the near absence of isolated fiber breaks away from the fracture plane, which suggest that stress concentration effects were strong near the fracture plane. Overall, an important outcome of the modeling and experimental efforts is believed to be the establishment of a direct relationship between the strain-to-failure of the matrix material and the strength utilization of fibers under longitudinal loading.

The 90-deg MMC did not provide any significant strength enhancement through heat treatment. A principal reason was the presence of an  $\alpha_2$  enriched zone, likely because of carbon pickup. A Nb coating on the fiber helped to retain the O and B2 phases around the fiber, and this did provide modest improvements in the strength and ductility of the 90-deg MMC.

The microstructure-property relations and the deformation mechanisms of the constituent phases of the O alloy were also studied to determine the roles played by the those phases and to help guide the selection of an appropriate heat treatment for the MMC. The B2 phase has wavy slip behavior with dimple fracture characteristics and is an important ingredient for imparting ductility to the matrix, thus increasing the strength utilization of the fibers. The  $\alpha_2/\alpha_2$  grain boundaries should be avoided because they are potent cracking sites. The O phase is more crack resistant, and, based on other studies, this phase is important for high-temperature transverse strength and creep resistance of MMCs.

The same heat treatment did not produce identical microstructures in the sheet, neat, and MMC specimens due to different levels of interstitials (carbon and oxygen). Thus, careful attention needs to be focused on this issue when devising heat treatments for microstructural and MMC strength improvements. In particular, carbon pickup from the fiber needs to be reduced; otherwise, attempts to improve the ductility of transversely loaded specimens may prove elusive.

## ACKNOWLEDGMENTS

This research was performed at the USAF Wright Laboratory Materials Directorate under Air Force Contract No.

F33615-91-C-5663 to UES, Inc. We thank Dr. A.K. Rai and Messrs. Mark Dodd, Eric Fletcher, Tony Houston, Tim Shock, and Joe Henry, UES, Inc., for their assistance with the TEM, heat treatment, metallography, testing, and microprobe analyses.

## REFERENCES

1. D. Banerjee, A.K. Gogia, T.K. Nandy, and V.A. Joshi: *Acta Metall.*, 1988, vol. 36, pp. 871-82.
2. B. Mozer, L.A. Bendersky, and W.J. Boettinger: *Scripta Metall.*, 1991, vol. 39, pp. 1959-69.
3. K. Muraleedharan, A.K. Gogia, T.K. Nandy, D. Banerjee, and S. Lele: *Metall. Trans. A*, 1992, vol. 23A, pp. 401-15.
4. R.G. Rowe, D. Banerjee, K. Muraleedharan, M. Larsen, E.L. Hall, D.G. Konitzer, and A.P. Woodfield: in *Titanium '92 Science and Technology*, F.H. Froes and I. Caplan, eds., TMS, Warrendale, PA, 1993, pp. 1259-66.
5. D. Banerjee: in *Intermetallic Compounds Principles and Practice*, J.H. Westbrook and R.L. Fleischer, eds., John Wiley & Sons Ltd., New York, NY, 1994, vol. 2, pp. 91-131.
6. P.R. Smith, W.J. Porter, W.J. Kralik, and J.A. Graves: *Metal Matrix Composites*, Proc. 10th Int. Conf. on Composite Materials, A. Poursartip and K.N. Street, eds., Woodhead Publishing Ltd., Vancouver, B.C., 1995, vol. 2, pp. 731-38.
7. P.R. Smith, J.A. Graves, C.G. Rhodes, M.R. James, and J.R. Porter: *Titanium Matrix Composites*, WL-TR-92-4035, Wright-Patterson Air Force Base, OH, 1992, pp. 115-45.
8. A.K. Gogia, T.K. Nandy, K. Muraleedharan, and D. Banerjee: *Mater. Sci. Eng.*, 1992, vol. A159, pp. 73-86.
9. S. Krishnamurthy, P.R. Smith, and D.B. Miracle: *Scripta Metall.*, 1994, vol. 31, pp. 653-58.
10. S.M. Russ, C.J. Boehlert, and D. Eylon: *Mater. Sci. Eng.*, 1995, vols. A192-A193, pp. 483-89.
11. M.J. Blackburn and M.P. Smith: *Improved Toughness Alloys Based on Titanium Aluminides*, WRDC-TR-89-4095, Wright-Patterson Air Force Base, OH, 1989, pp. 162-72.
12. D.B. Miracle, B.S. Majumdar, S. Krishnamurthy, and M. Waterbury: *Metal Matrix Composites*, Proc. 9th Int. Conf. on Composite Materials, A. Miravete, ed., Woodhead Publishing Ltd., 1993, pp. 610-24.
13. B.S. Majumdar, C.J. Boehlert, A.K. Rai, and D.B. Miracle: *High Temperature Ordered Intermetallic Alloys—VI*, Materials Research Society Symposia Proceedings, J. Horton, I. Baker, S. Hanada, R.D. Noebe, and D.S. Schwartz, eds., Materials Research Society, Pittsburgh, PA, 1995, vol. 364, pp. 1259-65.
14. B.S. Majumdar, C.J. Boehlert, and D.B. Miracle: *Orthorhombic Titanium Matrix Composites*, Proc. Orthorhombic Titanium Matrix Composites Workshop, WL-TR-95-4068, Wright-Patterson Air Force Base, OH, 1995, pp. 65-83.
15. C.J. Boehlert, B.S. Majumdar, and D.B. Miracle: *Fatigue and Fracture of Ordered Intermetallics II*, TMS Fall Meeting, T.S. Srivatsan, W. Soboyejo, and R.O. Ritchie, eds., TMS, Warrendale, PA, 1995, pp. 135-53.
16. W.A. Curtin: *J. Am. Cer. Soc.*, 1991, vol. 74, p. 2837.
17. C. Zweben and B.W. Rosen: *J. Mech. Phys. Solids*, 1970, pp. 189-206.
18. A.H. Kelly and N.H. Macmillan: *Strong Solids*, 3rd ed., Clarendon Press, Oxford, United Kingdom, 1986.
19. M.J. Iremonger and W.G. Wood: *J. Strain Analysis*, 1967, vol. 2.
20. B.S. Majumdar and D.B. Miracle: *J. Key Eng. Mater.*, 1996, vols. 116-117, pp. 153-72.
21. B.S. Majumdar, S.G. Warrier, T. Matikas, and D.B. Miracle: *Interfacial Engineering*, Materials Research Society Symposia Proceedings, E. Hall and E.B. Carter, eds., Materials Research Society, Pittsburgh, PA, 1996, in press.
22. J.M. Hedgepeth and P. Van Dyke: *J. Composite Mater.*, 1967, vol. 1, p. 294.
23. K. Muraleedharan: Ph.D. Thesis, Banaras Hindu University, Banaras, India, 1995.
24. D.B. Miracle, M.A. Foster, and C.G. Rhodes: in *Titanium '95*, Proc. 8th World Conf. on Titanium, P.A. Blenkinsop, W.J. Evans, and H.M. Flower, eds., The University Press, Cambridge, United Kingdom, 1996, vol. 1, pp. 372-79.
25. K. Muraleedharan, T.K. Nandy, D. Banerjee, and S. Lele: *Metall. Trans. A*, 1992, vol. 23A, pp. 417-31.
26. K. Muraleedharan, D. Banerjee, S. Banerjee, and S. Lele: *Phil. Mag.*, 1995, vol. 71 (5), pp. 1011-36.
27. S. Krishnamurthy: UES, Inc., Dayton, OH, unpublished research, 1996.
28. W.C. Revelos, J.W. Jones, and E.J. Dolley: *Metall. Trans. A*, 1995, vol. 26A, p. 1167.
29. S. Krishnamurthy and D.B. Miracle: UES, Inc., Dayton, OH, Wright-Patterson Air Force Base, OH, unpublished research, 1995.
30. S.M. Pickard and D.B. Miracle: *Mater. Sci. Eng.*, 1995, vol. A203, pp. 59-67.
31. S.L. Draper, P.K. Brindley, and M.V. Nathal: *Metall. Trans. A*, 1992, vol. 23A, pp. 2541-48.
32. R.A. MacKay, P.K. Brindley, and F.H. Froes: *JOM*, 1991, May, pp. 23-29.
33. A.S. Akkurt, G. Liu, and G.M. Bond: in *High-Temperature Ordered Intermetallic Alloys IV*, L.A. Johnson, D.P. Pope, and J.O. Stiegler, eds., Materials Research Society Symposia Proceedings, Materials Research Society, Pittsburgh, PA, 1991, vol. 213, pp. 455-60.
34. B.S. Majumdar and G.M. Newaz: *Phil. Mag.*, 1992, vol. 66 (2), pp. 187-212.
35. T.K. Nandy, R.S. Mishra, and D. Banerjee: *Scripta Metall.*, 1993, vol. 28, pp. 569-74.
36. S. Krishnamurthy: UES, Inc., Dayton, OH, unpublished research, 1995.
37. M.L. Gambone: in *Orthorhombic Titanium Matrix Composites*, Proc. Orthorhombic Titanium Matrix Composites Workshop, WL-TR-95-4068, Wright-Patterson Air Force Base, OH, 1995, pp. 341-52.
38. T. Nicholas: Wright-Patterson Air Force Base, OH, unpublished research, 1995.